LETTERS

Spatially resolved electronic and vibronic properties of single diamondoid molecules

YAYU WANG[1]*, EMMANOUIL KIOUPAKIS[1], XINGHUA LU[1], DANIEL WEGNER[1], RYAN YAMACHIKA[1],
JEREMY E. DAHL[2], ROBERT M. K. CARLSON[2], STEVEN G. LOUIE[1] AND MICHAEL F. CROMMIE[1]*

[1]Department of Physics, University of California at Berkeley, and Materials Sciences Division, Lawrence Berkeley Laboratory, Berkeley, California 94720-7300, USA
[2]MolecularDiamond Technology, Chevron Technology Ventures, Richmond, California 94802, USA
*e-mail: yywang@berkeley.edu; crommie@berkeley.edu

Diamondoids are a unique form of carbon nanostructure best described as hydrogen-terminated diamond molecules[1]. Their diamond-cage structures and tetrahedral sp^3 hybrid bonding create new possibilities for tuning electronic bandgaps, optical properties, thermal transport and mechanical strength at the nanoscale[1,2]. The recently discovered higher diamondoids[3,4] have thus generated much excitement in regards to their potential versatility as nanoscale devices[5–15]. Despite this excitement, however, very little is known about the properties of isolated diamondoids on metal surfaces, a very relevant system for molecular electronics. For example, it is unclear how the microscopic characteristics of molecular orbitals and local electron–vibrational coupling affect electron conduction, emission and energy transfer in the diamondoids. Here, we report the first single-molecule study of tetramantane diamondoids on Au(111) using scanning tunnelling microscopy and spectroscopy. We find that the diamondoid electronic structure and electron–vibrational coupling exhibit unique and unexpected spatial correlations characterized by pronounced nodal structure across the molecular surfaces. *Ab initio* pseudopotential density functional calculations reveal that much of the observed electronic and vibronic properties of diamondoids are determined by surface hydrogen terminations, a feature having important implications for designing future diamondoid-based molecular devices.

The [121]tetramantane diamondoid studied here consists of four diamond cages face-fused into a straight rod with a chemical formula $C_{22}H_{28}$ (ref. 3; see schematic structure in Fig. 1a). The 28 surface dangling carbon bonds are all saturated by hydrogen atoms. The [121]tetramantane molecules used here were extracted from petroleum and isolated and purified to a white crystalline powder with purity greater than 99% by weight. Purification procedures included distillation, thermal processing and both size- and shape-selective high-performance liquid chromatography, as described in ref. 4.

Tetramantane molecules were thermally evaporated onto a clean Au(111) substrate held at room temperature in ultrahigh vacuum. Under these conditions, the diamondoid molecules self-assemble into an ordered overlayer. Figure 1b shows the scanning tunnelling microscopy (STM) topography taken at $T = 7$ K of a sub-monolayer of tetramantane on Au(111) where the oval-shaped tetramantane molecules form a close-packed structure with lattice constants 11.4 Å × 8.3 Å (see red arrows) and an apparent height

of ~3.3 Å. The herringbone reconstruction of the Au(111) surface (the faint bright stripes) has negligible effect on the arrangement of the molecules. The formation of long-range ordering at room temperature implies high molecular mobility and weak bonding between the diamondoids and the Au(111) substrate.

To examine individual tetramantane diamondoids, we used the STM tip to manipulate the diamondoids from the edge of an island onto an empty Au(111) terrace at $T = 7$ K (ref. 16). Figure 1c,d shows STM topographs of the same individual diamondoid taken with different sample biases. The image taken at sample bias $V = +2$ V (Fig. 1c), which probes the unoccupied local electronic density of states (LDOS), exhibits pronounced line nodes across the molecular surface. In contrast, the image taken at -2 V (Fig. 1d) has less pronounced features, revealing a much weaker spatial dependence of the occupied electronic states. Tetramantane was found to have a number of different orientations on Au(111). Figure 2a shows STM images of three tetramantane diamondoids lying on Au(111) with different molecular orientations, as seen by the distinctive spatial patterns of the line nodes. Diamondoids can be switched between molecular orientations by dragging and rotating the tetramantane using the STM tip.

The local electronic structure of tetramantane diamondoid was probed by scanning tunnelling spectroscopy. Figure 3a shows the dI/dV spectra of the bare Au(111) substrate (black curve), and the spatially averaged dI/dV of a tetramantane diamondoid residing on Au(111) (blue curve). The main features of the two spectra are very similar, implying that the diamondoid makes a small contribution to the total surface electronic LDOS. Subtracting the Au background from the total dI/dV yields the contribution of tetramantane to the spectrum, which is shown by the red curve in Fig. 3a. The molecular electronic LDOS is quite low for the energy range from -2.5 eV to $+2.5$ eV, consistent with a highly insulating ground state having an energy gap $\Delta \geq 5$ eV about the Fermi level (E_F) (refs 6,9,14). Although no sharp resonances related to the highest occupied molecular orbital (HOMO) or the lowest unoccupied molecular orbital (LUMO) were observed, the gentle increase of dI/dV above E_F may represent the tail of the broadened LUMO level.

High-resolution dI/dV spectroscopy in the low bias range reveals a 'V'-like feature about E_F and two steep jumps in dI/dV at ± 356 mV (the upper panel of Fig. 3b). The numerical derivative of this curve (d^2I/dV^2) correspondingly shows two sharp antisymmetric peaks at ± 356 mV (the lower panel of Fig. 3b). This
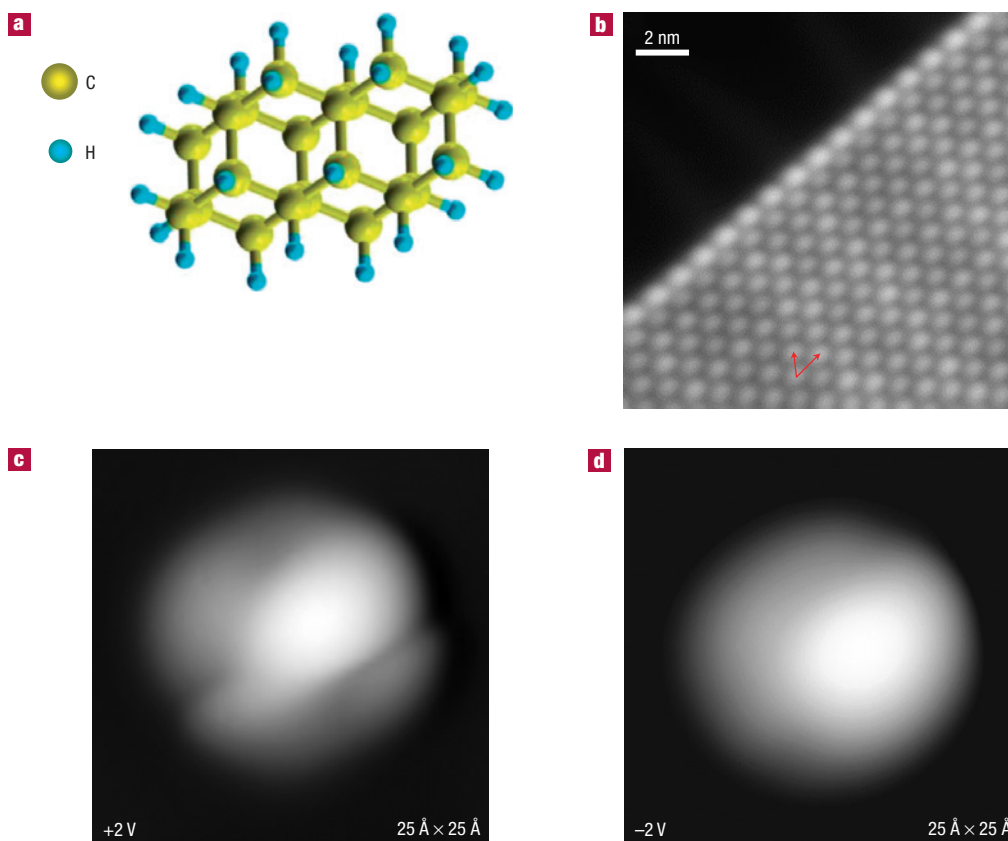
Figure 1 STM topography of tetramantane molecules. a, The structural model of [121]tetramantane ($C_{22}H_{28}$). **b**, Constant-current topograph of a sub-monolayer of tetramantane on Au(111) taken with sample bias $V = 2.0\,V$ and tunnelling current $I = 50\,pA$. The long axis of the tetramantane molecules is aligned along the atomic step edge of the Au(111) surface. The red arrows indicate the basis vectors of the ordered structure. **c,d**, STM topographs ($25\,Å \times 25\,Å$) of an individual tetramantane molecule taken with sample bias of $+2.0\,V$ (**c**) and $-2.0\,V$ (**d**).

is the classic hallmark of inelastic electron tunnelling spectroscopy (IETS), in which the electronic excitation of molecular vibrations opens a new tunnelling channel[17]. The 356 meV vibrational energy seen here for tetramantane corresponds to the stretch mode of a C–H bond, as has been observed in numerous other hydrocarbons[18]. The 'V'-like feature in dI/dV between the $\pm356\,mV$ jumps might also be related to inelastic tunnelling of electrons interacting with quasi-continuous, low-frequency vibrations of the tetramantane[19].

To understand the microscopic characteristics of electron–vibration coupling across the surface of a single diamondoid, we carried out spatially resolved IETS across individual tetramantane molecules[20–22]. We find that the pronounced inelastic signals at $\pm356\,mV$ only exist on certain parts of the molecules, and become negligibly small elsewhere. Figure 4a shows the d^2I/dV^2 maps of the C–H stretch mode for three individual diamondoids having different orientations, demonstrating unambiguously that the vibronic coupling strength is strongly localized to narrow slices on the molecular surfaces. Comparing the IETS maps of the diamondoids with their respective topographs (Fig. 4b) reveals an anticorrelation between the elastic and inelastic tunnelling channels: the IETS intensity peaks sharply at the topographic line nodes where elastic tunnelling is suppressed.

Such localization of the inelastic signal is unexpected because the 28 C–H bonds surrounding the tetramantane exhibit a dense and nearly uniform surface termination. Moreover, it

might naively be expected that enhanced elastic tunnelling goes hand-in-hand with enhanced inelastic tunnelling (as there is then more electron density to excite molecular vibrations)[23], opposite to the anticorrelation observed here.

To understand this behaviour, we have carried out *ab initio* pseudopotential density functional theory (DFT) calculations within the local density approximation (LDA) for a [121]tetramantane molecule on Au(111). We carried out these calculations first by using a plane-wave pseudopotential (PW-PP) code to obtain the properties of the isolated molecule[24]. We then modelled the gold surface by three layers of 56 gold atoms each (in a supercell geometry) and calculated the properties of the combined diamondoid/Au(111) system using the SIESTA code[25], which uses a localized basis set, because the use of plane waves for the combined calculation would be much more expensive. We have checked thoroughly that the SIESTA code produces results consistent with the plane-wave code when an appropriate set of ghost atoms is introduced (see Supplementary Information, Fig. S1).

Figure 3c shows the schematic energy diagram of the system under investigation. The theoretical Kohn–Sham HOMO–LUMO gap of the isolated molecule is found to be 5.2 eV, which is an underestimation of the true quasiparticle gap[26]. The electron affinity and ionization potential were obtained by computing the total energy of singly charged molecules, and were calculated to be $-0.3\,eV$ and 7.6 eV respectively. The values of the HOMO–LUMO gap and the electron affinity/ionization potential gap agree well
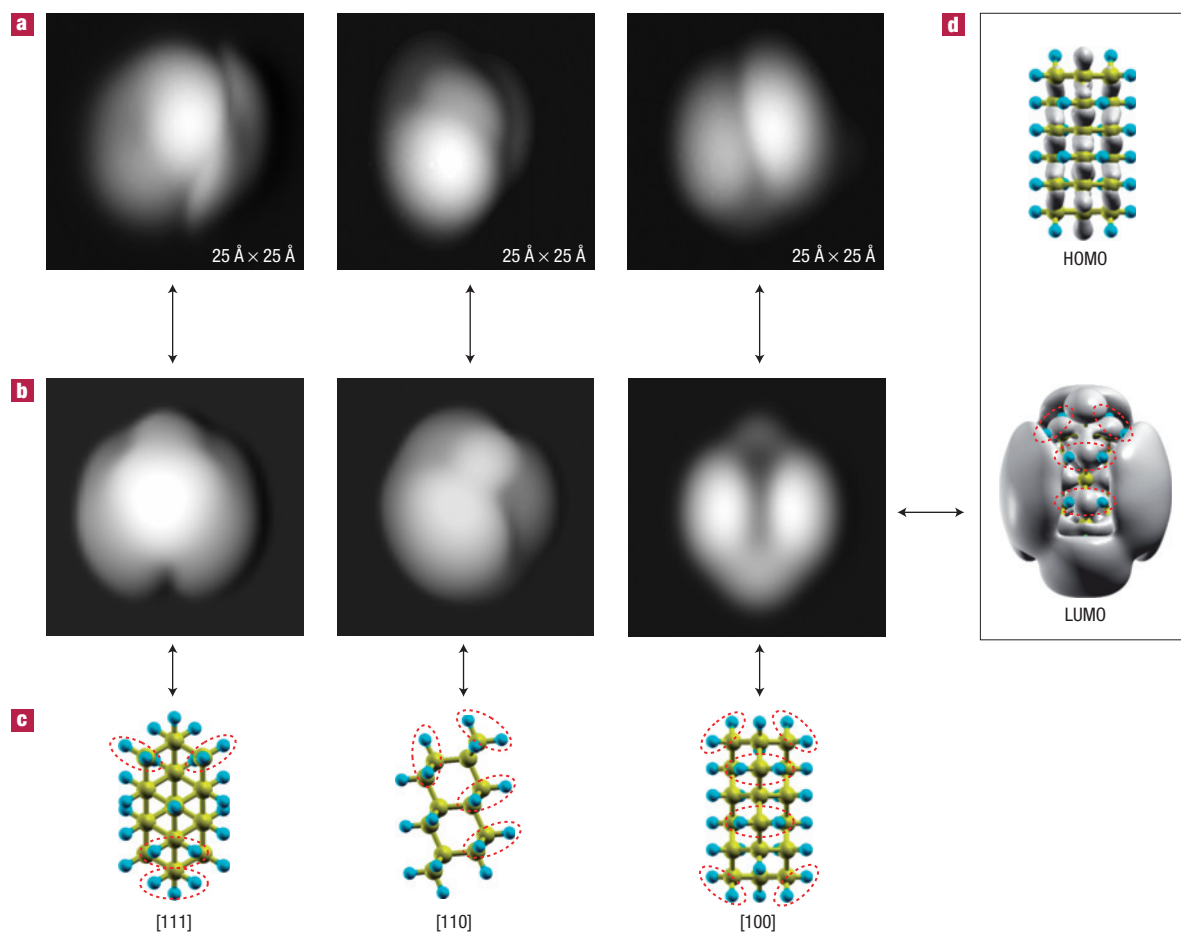
Figure 2 STM images and DFT simulations of individual tetramantane molecules. a, Positive-bias ($V = +2.0\,V$) STM images of three individual tetramantane molecules with different molecular orientations. **b**, DFT-simulated LUMO-level STM topographs of the three isolated tetramantane molecules. **c**, Top view of the schematic structure of the three tetramantane molecules lying on the substrate with their z axis oriented along the diamond crystallographic [111], [110] and [100] directions, respectively. Dashed red lines highlight the doubly hydrogenated CH_2 sites. **d**, DFT-calculated isosurfaces of the HOMO and LUMO electronic wavefunction square at a value corresponding to 50% of the charge of the state for the third molecule shown in **a**.

with quantum Monte Carlo calculations reported previously for the larger diamondoid $C_{29}H_{35}$ (ref. 6). We find that diamondoids have an intrinsic negative electron affinity, as first pointed out in ref. 6, which makes them promising candidates for electron-emission devices. Recent photoemission data have indeed demonstrated strong monochromatic low-kinetic-energy electron emission in diamondoid monolayers on Au(111) (ref. 15).

Figure 3d shows the DFT-calculated electronic density of states of a tetramantane molecule when the effect of the Au(111) surface is included. The LDA HOMO and LUMO levels are located at approximately $-1.0\,eV$ and $+3.9\,eV$ relative to E_F, leading to a reduced Kohn–Sham energy gap of 4.9 eV due to screening from the metal substrate. The broadened LDOS of the LUMO level extends into the energy gap as a shallow tail, consistent with the experimental dI/dV curve. However, the theoretical HOMO resonance at $-1.0\,eV$ is not observed in the experiment down to $-2.5\,eV$.

This discrepancy can be understood by calculating the spatial distribution of the wavefunctions of the molecular electronic states. Figure 2d shows the calculated isosurfaces of the HOMO and LUMO electronic wavefunction square at a value corresponding to 50% of the charge of each state for an isolated tetramantane

molecule with a particular molecular orientation. The occupied electronic states are concentrated on the centres of the C–C bonds, reflecting the spatial localization of the sp^3 bonding orbitals. Such confined states are difficult for STM to detect (with the tip at several ångströms above the molecule), which explains the weak spatial features of the negative-bias image and the absence of the HOMO resonance in the dI/dV spectrum. The calculated LUMO orbital, on the other hand, is much more delocalized in space and exhibits pronounced spatial variations similar to those seen experimentally. The extended LUMO state has previously been shown to be responsible for the negative electron affinity and anomalous quantum size effect of the diamondoids[6].

Closer comparison of the tetramantane LUMO isosurface and the diamondoid molecular structure uncovers an intriguing trend: the strong spatial variation of the electronic states is closely related to the nature of the surface hydrogen terminations. The large, delocalized LUMO state density exists only at the 12 singly hydrogenated CH sites, and forms smooth patches in these CH-rich areas. The 8 doubly hydrogenated CH_2 sites (highlighted by dashed red lines in Fig. 2c), in contrast, exhibit little electronic density and form depressions in the LUMO isosurface plot. This is caused by the peculiar formation of the LUMO orbitals on the CH_2 sites.
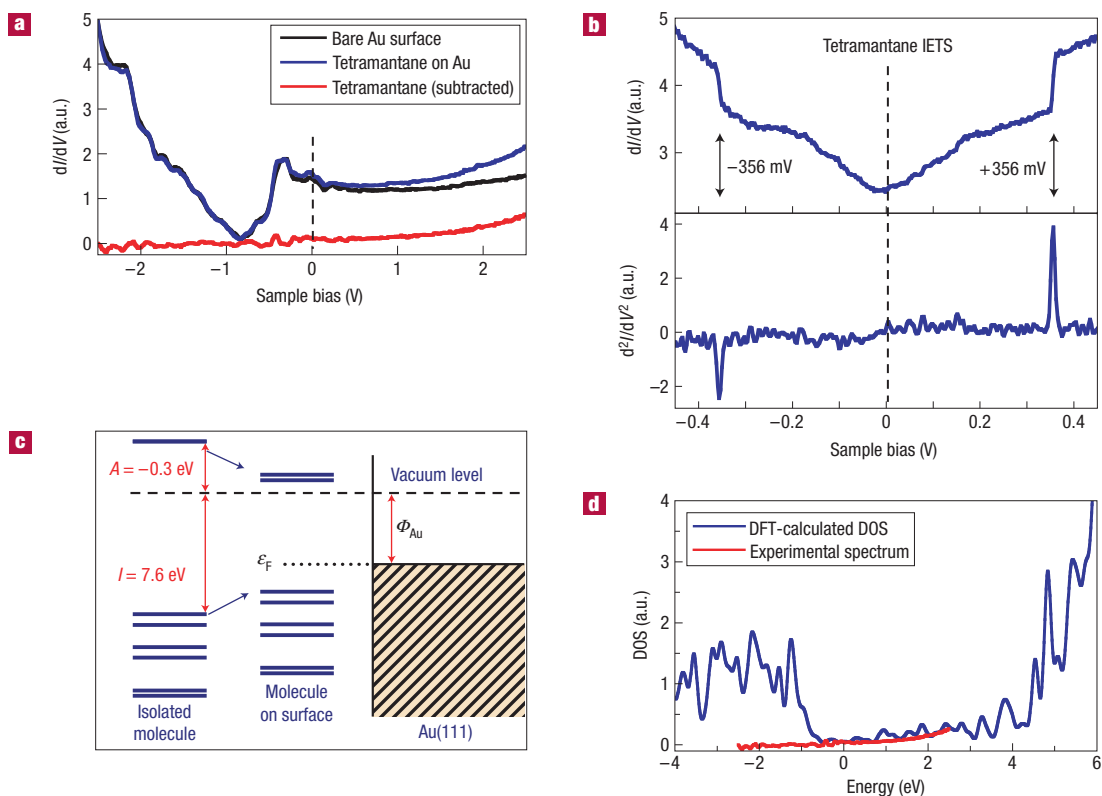
Figure 3 dI/dV spectroscopy of tetramantane molecules. a, dI/dV spectra of bare Au(111) (black curve) and a tetramantane molecule on Au (blue curve). The difference (red curve) represents the contribution of tetramantane. **b**, Low-bias dI/dV spectrum on tetramantane shows two steps at ±356 mV (upper panel). The numerically derived d^2I/dV^2 curve shows two antisymmetric peaks at ±356 mV (lower panel). **c**, Schematic electronic energy diagram of tetramantane. **d**, The calculated density of states of a tetramantane molecule on Au(111) compared with the experimental dI/dV spectrum.
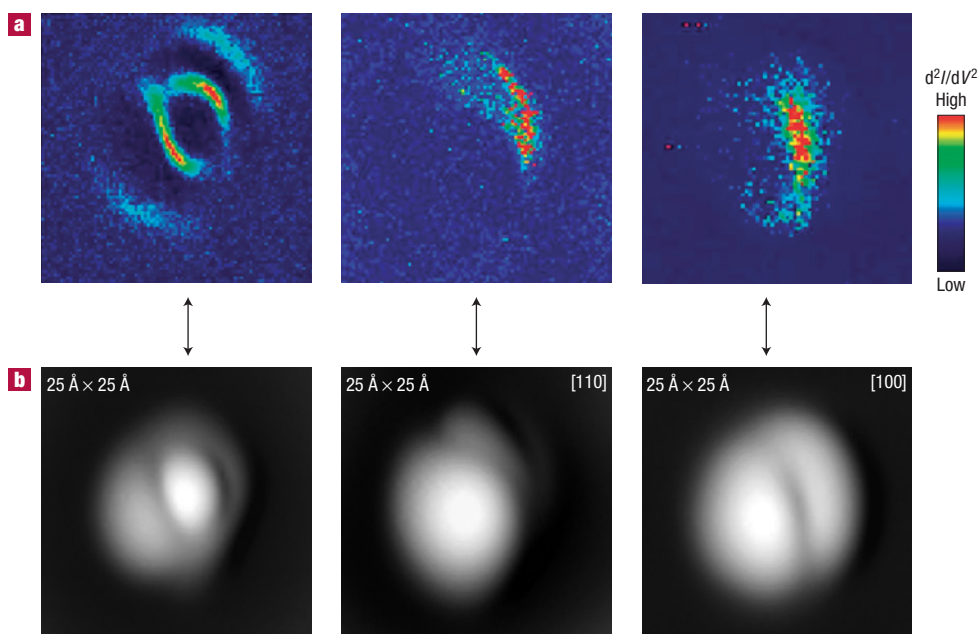

Figure 4 Spatial maps of the IETS intensity. a, STM inelastic tunnelling d^2I/dV^2 maps of the C–H stretch mode (0.36 V) of three tetramantane molecules with different orientations. The inelastic signal is strongly localized to narrow slivers on the molecular surface. **b**, STM topographs (at $V = +2.0$ V) of the same molecules shown in **a** reveal that the inelastic intensity peaks sharply at the LUMO-level topographic line nodes. The left-most molecule has an orientation that deviates from high symmetry, and the other two molecules are orientated along the [110] and [100] directions respectively.

Here, the most relevant LUMO wavefunction, the so-called $\sigma^*_{CH_2}$ orbital, is constructed by a linear combination of the antibonding wavefunctions formed between the two canted carbon sp^3 orbitals and between the two hydrogen s orbitals[27]. The derived $\sigma^*_{CH_2}$ wavefunction has a pronounced node on the mirror plane that bisects the H–C–H complex.

This behaviour can be seen better in Fig. 2b, which shows three calculated LUMO-level STM topographs of isolated tetramantane molecules. The schematic top views in Fig. 2c reveal that the three molecules lie on the substrate with their z axis oriented along the diamond crystallographic [111], [110] and [100] directions, respectively (from left to right). These simulated images match well the essential features of the corresponding STM images taken at +2.0 V (Fig. 2a). The excellent agreement clearly demonstrates that the pronounced nodal features found in the tetramantane STM images result from suppressed LUMO electronic state density at the doubly hydrogenated CH_2 sites.

Next, we turn to the inelastic tunnelling spectroscopy. The strength of electronic coupling to the C–H stretch mode has been evaluated by calculating the change of the electronic energy eigenvalues with respect to displacements along the canonical phonon coordinates[22,23]. Out of the 28 C–H stretch modes, we have identified three that interact strongly with tunnelling electrons within 15 meV of the experimental signal. The question remains, however, as to why the experimental IETS signal is enhanced in the CH_2-terminated regions of the diamondoid and suppressed elsewhere. We postulate that this occurs because the CH_2 region has a denser concentration of C–H bonds, and hence a higher probability of electronic interactions with the C–H stretch mode compared with the singly hydrogenated CH region. Unique local vibrational features at the CH_2 sites may also enhance the strength of electron–vibrational coupling in these regions.

Our unified STM and DFT investigations show that the important electronic and vibronic properties of higher diamondoids are determined by microscopic differences in the surface hydrogen termination where the singly hydrogenated CH sites and doubly hydrogenated CH_2 sites behave very differently. The pronounced nodal (antinodal) features in STM topography (IETS) originate exclusively from the CH_2 sites. This information should help to structurally optimize the effect of C–H stretch vibrations on electron transport in future molecular devices. Our results also suggest that selective substitution of H atoms on the singly or doubly hydrogenated sites may lead to very different functionalities for electronic devices, taking advantage of novel diamondoid properties such as negative electron affinity, tuned electrical conductivity and optical absorption, and heat flow.

METHODS

SAMPLE PREPARATION AND STM EXPERIMENTS

In our experiments, tetramantane molecules were thermally deposited in ultrahigh vacuum from a Knudsen cell evaporator onto a clean Au(111) surface held at room temperature. STM measurements were carried out using a home-built system with a polycrystalline PtIr tip operated at a cryogenic temperature $T = 7\,K$. STM topography was carried out in constant-current mode, and dI/dV spectra and images were measured through lock-in detection of the a.c. tunnelling current driven by a 450 Hz, 1–10 mV (r.m.s.) signal added to the junction bias (defined as the sample potential referenced to the tip) under open-loop conditions. The molecular manipulation method used here is the 'sliding' technique[16] with typical manipulation parameters $V = 5\,mV$ and $I = 1\,nA$.

THEORETICAL CALCULATIONS

Our calculations were carried out using DFT in the LDA using the functional of Perdew and Zunger[28]. We used the PW-PP method[24] using Troullier–Martins norm-conserving pseudopotentials[29]. We used a 60 Ry plane-wave cutoff and a rectangular simulation cell of $40 \times 40 \times 50\ a_B$ (a_B is the Bohr radius). For our SIESTA calculations[25], we used the same pseudopotentials as in our PW-PP calculations and a double-ζ polarized basis. We extended the basis set by introducing ghost atoms in the vacuum region and by including two s-type orbitals per ghost atom. We have carried out thorough checks to verify that the SIESTA results converge with those obtained by the PW-PP method, as discussed in detail in the Supplementary Information.

References

1. Marchand, A. P. Diamondoid hydrocarbons—delving into nature's bounty. *Science* **299**, 52–53 (2003).
2. Raty, J. Y. & Galli, G. Ultradispersity of diamond at the nanoscale. *Nature Mater.* **2**, 792–795 (2003).
3. Dahl, J. E., Liu, S. G. & Carlson, R. M. K. Isolation and structure of higher diamondoids, nanometer-sized diamond molecules. *Science* **299**, 96–99 (2003).
4. Dahl, J. E. *et al.* Isolation and structural proof of the large diamond molecule, cyclohexamantane ($C_{26}H_{30}$). *Angew. Chem. Int. Edn* **42**, 2040–2044 (2003).
5. McIntosh, G. C., Yoon, M., Berber, S. & Tomanek, D. Diamond fragments as building blocks of functional nanostructures. *Phys. Rev. B* **70**, 045401 (2004).
6. Drummond, N. D., Williamson, A. J., Needs, R. J. & Galli, G. Electron emission from diamondoids: A diffusion quantum Monte Carlo study. *Phys. Rev. Lett.* **95**, 096801 (2005).
7. Lu, A. J., Pan, B. C. & Han, J. G. Electronic and vibrational properties of diamondlike hydrocarbons. *Phys. Rev. B* **72**, 035447 (2005).
8. Richardson, S. L., Baruah, T., Mehl, M. J. & Pederson, M. R. Theoretical confirmation of the experimental Raman spectra of the lower-order diamondoid molecule: Cyclohexamantane ($C_{26}H_{30}$). *Chem. Phys. Lett.* **403**, 83–88 (2005).
9. Willey, T. M. *et al.* Molecular limits to the quantum confinement model in diamond clusters. *Phys. Rev. Lett.* **95**, 113401 (2005).
10. Filik, J. *et al.* Raman spectroscopy of nanocrystalline diamond: An *ab initio* approach. *Phys. Rev. B* **74**, 035423 (2006).
11. Fokin, A. A. *et al.* Reactivity of [1(2,3)4]pentamantane (T-d-pentamantane): A nanoscale model of diamond. *J. Org. Chem.* **71**, 8532–8540 (2006).
12. Oomens, J. *et al.* Infrared spectroscopic investigation of higher diamondoids. *J. Mol. Spectrosc.* **238**, 158–167 (2006).
13. Schreiner, P. R. *et al.* Functionalized nanodiamonds: Triamantane and [121]tetramantane. *J. Org. Chem.* **71**, 6709–6720 (2006).
14. Willey, T. M. *et al.* Observation of quantum confinement in the occupied states of diamond clusters. *Phys. Rev. B* **74**, 205432 (2006).
15. Yang, W. L. *et al.* Monochromatic electron photoemission from diamondoid monolayers. *Science* **316**, 1460–1462 (2007).
16. Eigler, D. M. & Schweizer, E. K. Positioning single atoms with a scanning tunnelling microscope. *Nature* **344**, 524–526 (1990).
17. Stipe, B. C., Rezaei, M. A. & Ho, W. Single-molecule vibrational spectroscopy and microscopy. *Science* **280**, 1732–1735 (1998).
18. Ho, W. Single-molecule chemistry. *J. Chem. Phys.* **117**, 11033–11061 (2002).
19. Kirtley, J. R., Washburn, S. & Scalapino, D. J. Origin of the linear tunneling conductance background. *Phys. Rev. B* **46**, 336–346 (1992).
20. Stipe, B. C., Rezaei, H. A. & Ho, W. Localization of inelastic tunneling and the determination of atomic-scale structure with chemical specificity. *Phys. Rev. Lett.* **82**, 1724–1727 (1999).
21. Hahn, J. R., Lee, H. J. & Ho, W. Electronic resonance and symmetry in single-molecule inelastic electron tunneling. *Phys. Rev. Lett.* **85**, 1914–1917 (2000).
22. Grobis, M. *et al.* Spatially dependent inelastic tunneling in a single metallofullerene. *Phys. Rev. Lett.* **94**, 136802 (2005).
23. Lorente, N. & Persson, M. Theory of single molecule vibrational spectroscopy and microscopy. *Phys. Rev. Lett.* **85**, 2997–3000 (2000).
24. Ihm, J., Zunger, A. & Cohen, M. L. Momentum-space formalism for the total energy of solids. *J. Phys. C* **12**, 4409–4422 (1979).
25. Soler, J. M. *et al.* The SIESTA method for *ab initio* order-N materials simulation. *J. Phys. Condens. Matter* **14**, 2745–2779 (2002).
26. Hybertsen, M. S. & Louie, S. G. Electron correlation in semiconductors and insulators: Band gaps and quasiparticle energies. *Phys. Rev. B* **34**, 5390–5413 (1986).
27. Jorgensen, W. L. & Salem, L. *The Organic Chemist's Book of Orbitals* (Academic, New York, 1973).
28. Perdew, J. P. & Zunger, A. Self-interaction correction to density-functional approximations for many-electron systems. *Phys. Rev. B* **23**, 5048–5079 (1981).
29. Troullier, N. & Martins, J. L. Efficient pseudopotentials for plane-wave calculations. *Phys. Rev. B* **43**, 1993–2006 (1991).